Origami-patterned capacitor with programmed strain sensitivity

Kristen L. Dorsey, HuiYing Huang, and Yuhan Wen

Origami patterns have previously been investigated for novel mechanical properties and applications to soft and deployable robotics. This work models and characterizes the mechanical and electrical properties of origami-patterned capacitive strain sensors. Miura-patterned capacitors with different fold angles are fabricated with a silicone body and foil electrodes. The planar strain sensitivity ratio is tunable from 0.3 to 0.5 with fold angles, while all-soft patterns demonstrate low mechanical tunability through fold angle. We conclude by offering recommendations for designing and modeling future origami-patterned soft material sensors.

Keywords – origami, Miura, strain sensor, stretchable, silicone, tunable

1 Introduction

Origami has garnered interest within the multifunctional materials and robotics research communities for its novel mechanical properties, including auxetic behavior (i.e., negative Poisson's ratios) [1], programmable stiffness [2] [3], and the ability to locomote [4], [5], or shape-change [6], [7], [8] by folding and unfolding in response to control signals or contact with objects. These properties bring variable stiffness and deployable capabilities to soft robotics and actuators fabricated in soft materials such as paper, fabric, and rubber [9], [10], [11].

As soft or flexible systems such as soft robots are applied in progressively less structured environments, mechanical sensors within such systems, which provide information about actuator positions and contact with the environment or objects, must meet the demands of sensitivity, selectivity, and range imposed by the intended application. Sensors used to measure the deformation of actuators may need to have large strain sensitivity but low pressure sensitivity, while sensors used to determine environmental contact may need the opposite properties.

Recent work has successfully used the morphology of a sensor to tune its sensitivity or selectivity through auxetic [12, 13] or variable stiffness [14] frames, voids, channels, and kirigami (i.e., cut patterns) [15, 16, 17], and pyramids [18, 19]. By modifying the response of the electrical material to mechanical deformation, these structures change the sensitivity [13] or yield strain [20] of the sensor. Such designs modify the sensor response without changing the underlying materials. In origami-patterned systems, a similar approach could apply a sensing modality to an origami structure to create an actuator with a sense of self, such as in previously demonstrated sensorized robotic origami and origami actuators [9, 10, 11]. If the sensing properties of such origami patterns were well understood, origami actuators could be self-sensing simply by adding sensing functionality to the actuator.

Predicting or programming an origami-patterned sensor's response requires a strong understanding of the pattern fold kinematics and the deformation of the sensitive materials. The mechanical properties of origami patterns [1], [21], [22], [23], and their applications to actuators [24], [25], [2], [26], [27], and grippers [28], have been modeled and investigated primarily in flexible yet inextensible materials: paper, cardboard, metal foils, and flexible, 3D printed thermoplastics [29], [30], where the folding and unfolding of pattern faces is of primary interest. The compliance of pattern faces (rather than folds) also contributes to the pattern deformation ([21]] by behaving as an additional hidden fold.

Origami fabricated from stretchable materials (e.g., rubber) [2, 6, 31] adds an additional layer of complexity to analysis and design. As a load is imposed on the structure, the pattern may bend or stretch at pattern faces and folds. Some previous work has investigated these responses in soft materials. Kim et al. [31] fabricated and analyzed inflatable origami structures, such as a bio-inspired origami eel. This structure, fabricated from layered sheets of silicone elastomer, mechanically deforms in two modes: the first is an unfolding motion at the hinges of the sheet, followed by elastomer stretching. The majority of the extension takes place in the origami unfolding. Paez et al. [32] fabricated an elastomeric pneumatic actuator with paper origami shell and demonstrated the ability to tune the bending response of the actuator and its actuation pressure by changing the paper weight and fold angles.

In this work, we design and characterize an origami-patterned elastomeric capacitor. Our objectives are to i) investigate the validity of existing models in predicting the behavior of origami patterns fabricated in soft elastic materials (e.g., silicone rubber), and ii) determine the suitability of origami patterns for modifying soft-material sensor properties. We simulate the expected mechanical and electrical properties of an origami-patterned capacitor using analytical models of the kinematics and displacement of electrodes. Using these models, we select, fabricate, and characterize designs with the same pattern and three fold angle combinations. We conclude with design recommendations for future origami-patterned sensors and sensorized actuators. To the authors' knowledge, this work is the first to investigate the Miura pattern's utility to sensing in soft materials.

2 Design of a Miura capacitive sensor

2.1 The Miura pattern

A frequently investigated origami pattern is the Miura fold [33] (Fig. \blacksquare a), which is a series of repeated, chevron-like structures. Each cell within the Miura fold (Fig. \blacksquare b) can be described as a set of four coincident parallelograms offset by pattern angles α and θ , where α is constrained from 0° to 90° and θ from 0° to 180° . Selecting these pattern angles changes the Poisson's ratios and stiffnesses \blacksquare 21 23 and controls the deformation of the pattern.

While the faces of each cell in the Miura pattern may have unequal sides, this work focuses on equal parallelogram pattern faces with length L (i.e., rhombus faces) to reduce the design space. Analytical models [1], [21] have been developed to describe the pattern's kinematics in inextensible materials, and a brief overview is given here. Each dimension of a Miura cell can be described by L, θ , and α . Using the nomenclature from Wei et al. [21], the width and length of each cell (Fig. [1b]) are

respectively

$$w = 2L\sin\alpha\sin\left(\frac{\theta}{2}\right) \tag{1}$$

and

$$l = 2L\cos\alpha \left(1 - \sin^2\alpha \sin^2\left(\frac{\theta}{2}\right)\right)^{-1/2} \tag{2}$$

The influence of α and θ on cell morphology is shown in Fig. Ic. Angle α determines the acuteness of each rhombus face; increasing α while holding θ constant increases the cell width and height while decreasing the length. Increasing θ while holding α constant increases both the width and length of each cell while decreasing the height. As θ approaches 180° , the pattern approaches a flat sheet. Once fabricated, the pattern's α and L are fixed, while θ , l, and w vary as the cell is deformed.

Fabricating the Miura pattern places additional practical constraints on the pattern's two fold angles θ and β . In processes that deposit a conformal material over a template (e.g., casting, thin film processes), an acute angle between cell faces would pose challenges for sufficient sidewall coverage and de-molding the pattern from the template. We assume that θ and $\beta > 60^{\circ}$ will be sufficiently obtuse for pattern fabrication (such as in a de-molding process). The potential design space is shown in Fig. 11 as a map of each α , θ pair and the resultant β . While fabrication does not impose practical limits on the upper bound of the θ or β range, the pattern becomes more planar as either angle approaches 180° and limits the advantages of the origami pattern over a planar sensor. The maximum strain possible through unfolding is shown in Fig. 11.

In an inextensible material that may only fold or unfold at the pattern angles, increasing either l or w also increases the other dimension, θ , and β , while the pattern height decreases. By integrating resistive or capacitive modalities into the pattern, the relative position of each face (and therefore the pattern extension) could be detected. Selection of the initial α and θ angles tunes the sensor response to length or width extension by changing the initial pattern face orientation.

2.2 The Miura capacitor

A capacitance sensing mode in a Miura-patterned capacitor is investigated by applying electrodes onto the pattern faces. Capacitance sensing is selected over other modalities due to the ease of measurement and ability to modify sensitivity through pattern angles. To fabricate the capacitor, electrodes are placed on opposing face of the pattern with a fractional offset δ from the top and bottom of each cell. The gap between electrodes varies as the pattern is strained and the cells deform. By calculating the change in electrode-to-electrode distance for a change in l or w (i.e., strain in x or y), the change in capacitance may be estimated. Fig. 2a labels the variables of the capacitor.

Here, we build upon existing models of the Miura pattern kinematics [1] [21] to estimate the change in capacitance with strain applied to x or y. We begin by modeling the effects of x-axis strain. An undeformed cell has length l_0 and width w_0 (Fig. [2b]). For a cell that deforms purely by unfolding at each pattern crease, strain applied to the x-axis ε_x will result in a new triangle base length l_{new} (Fig. [2b]) such that

$$l_{new} = l_0(1 + \varepsilon_x) \tag{3}$$

where l_0 is the unstrained length of a cell. In pure unfolding, the length of the triangle base (l_{new}) and the strained cell length (l_t) are the same. If the sensor is made from an extensible material (e.g., silicone elastomer), however, it is likely to deform by both stretching and unfolding. The fraction of extension due to stretching may be encapsulated by a variable κ_x such that

$$l_{new} = l_0(1 + \varepsilon_x(1 - \kappa_x)) = l_0 + (l_t - l_0)(1 - \kappa_x)$$
(4)

and

$$d = l_0 \kappa_x \varepsilon_x = (l_t - l_0) \kappa \tag{5}$$

where d is the electrode-to-electrode spacing at the top of the cell. Using the values for l_{new} and d with strain, the capacitance change with deformation may be estimated. The gap between the electrodes at some position ζ from the top of the electrode face is

$$g = \frac{l_{new}}{2L}\zeta + d\tag{6}$$

and the capacitance C of each cell (without the fringing field) is

$$C = \int_{\delta L}^{(1-\delta)L} \frac{2\epsilon_0 L}{g} d\zeta \tag{7}$$

where δ is some fractional offset of each electrode from the edge of the cell. The capacitance of N cells is then

$$C = \frac{4N\epsilon_0 L^2}{l_{new}} \ln\left(\frac{(1-\delta)l_{new} + 2d}{\delta l_{new} + 2d}\right)$$
(8)

The effect of strain in the y-axis, ε_y , follows similar principles but is modified by the fabrication process. The foil electrodes, which do not allow the elastomer to stretch, connect one cell to its neighbor in the y direction. Therefore, there is no stretch in y, effectively collapsing to $\kappa_y = 0$ for all cases. The strained pattern width becomes

$$w_{new} = w_0(1 + \varepsilon_y) \tag{9}$$

The strained base length l_t may be calculated from eq. [2] and the value of w_{new} , with values for l_{new} and d calculated from eqs. [4] and [5].

In designing tunable sensors, several factors become critical for performance. One metric is the relative capacitance change $\Delta C_y/\Delta C_x$. Fig. 2d is a series of heatmaps that display the relative change in capacitance after a 5% strain applied in x or y. Values for κ_x of 0.05, 0.5, and 0.95, corresponding to predominantly unfolding, equal unfolding and stretching, and predominantly stretching, are displayed. All three heatmaps use a value $\kappa_y = 0$ due to the inextensible electrode constraint.

The predicted capacitance change is dependent on initial fold angles and ranges from 20 times higher in the x axis to 5 times higher in the y axis. The largest range results for predominantly unfolding ($\kappa_x \approx 0$). For all κ_x conditions, the highest

relative response (i.e., highest y-axis sensitivity) occurs in the region where θ and α are large.

A second sensor metric is the available sensing range, which is limited by the maximum extension that the pattern can undergo before becoming a planar sheet. The range is largest when θ is small. In the x axis, if θ is held constant, a larger α increases the sensing range.

The pattern angles and relative capacitance change at 5% strain are shown in Table Π . Given the range and relative sensitivities predicted by the model, three sets of angles were chosen: A, B, and C. These patterns were chosen for their range of strain sensitive ratios, maximum strain ranges, and to explore the tuning space enabled by α and θ . The model estimates that design A will have the largest relative sensitivity in y and the smallest range, while design C will have the largest relative sensitivity in x and the largest range.

2.3 Pattern and sensor fabrication

Elastomers and other soft materials have been patterned into origami structures through self-folding approaches [5] [34] [35], laser machining [36], casting and direct templating [6] [28] [37] [38], and 3D printing [29] [30] [39]. Here, we mold silicone elastomer precursors into custom molds to form the pattern and later apply foil electrodes once the material has cured to form the capacitive sensor. The process flow is shown in Fig. [3]

The mold designs are drawn using a custom CAD script (Fusion 360, Autodesk) that generates the pattern based on the face length and angles α and β . From the CAD drawing, a mold set with one tray and two lids are generated. One lid (1-mm) is sized to mold a pattern with thickness of 1 mm, and the other lid (2-mm) is sized to mold a pattern with the same α and θ_0 values but thickness of 2 mm. Each mold is 3D-printed through fused deposition modeling (UPrint SE, Stratasys) in acrylonitrile butadiene styrene (ABS) plastic.

Before casting, the template tray and lids are sprayed with a release agent (Ease Release 200, Reynolds Advanced Materials) and left for 10 min. To fabricate the elastomer-only patterns, liquid silicone precursors (Ecoflex 00-30, Smooth-On), manually mixed equally by weight, were poured into the template tray and left for 10 min to degas. The 2 mm lid is pressed onto the bottom tray using large binder clips and the elastomer is cured at room temperature inside the mold for 4 h before removing the lid.

To form patterns with electrodes, the silicone is patterned and cured using the steps described for the elastomer-only patterns, using the 1-mm lid rather than the 2-mm lid. Al foil tape with a thickness of 0.05 mm (K Flex) is cut into electrodes using a computer-controlled cutting machine (Maker, Cricut) using a revision of the custom Miura CAD script. The tape backing is removed, and the adhesive side of the tape is applied to the 1-mm lid to form the origami pattern. After the foil tape is adhered to the lid and manually shaped to the origami pattern, the adhesive is dissolved by spraying isopropanol over the electrode-lid assembly and allowing the isopropanol to evaporate for 30 min. A thin layer of liquid elastomer precursors is brushed over the cured silicone inside the tray mold. This new silicone layer is partially cured for 20 min to form a tacky adhesive layer, and the electrodes are applied to the pattern by inverting the lid and applying gentle pressure. After an additional 12 h cure, the 1-mm lid is demolded, additional liquid elastomer mixed equally by weight is poured into the tray, and the 2-mm lid is fixed

to the top of the tray with binder clips. This final step encases the electrodes in elastomer and forms the sensor. A completed device of each pattern is shown in Fig. [4].

3 Results

3.1 Mechanical response

To characterize the strain response, one end of each pattern is displaced in x or y (Fig. 5a), with the mean of each data set in the bolded line and one standard deviation shown using the shaded region. Four samples of each pattern, with (foil-elastomer, F) and without electrodes (elastomer-only, E), are strained to 20% along the x or y axis at a rate of 1 mm/s using a mechanical characterization tester (5542, Instron). Samples are loaded into the tester using pneumatic grips on the cross-heads and custom clips to hold the flat silicone edge of each sample.

In the elastomer-only patterns, patterns A, B, and C have similar stiffnesses in the x axis. In the y axis, the A pattern is stiffest and pattern C is the most compliant. Each pattern is approximately 1.5 times stiffer in the y axis over the x axis. Embedding foil electrodes within the pattern approximately doubles the stiffness. The same order of pattern compliance from C (most compliant) to A (stiffest) is preserved when the foil is embedded. The device-to-device variation in stiffness also increases from the elastomer-only to foil-elastomer samples.

The loading and unloading response in x (Fig. 5b) agrees with the responses observed in Figure 5a: pattern A is stiffest and pattern C is most compliant. Samples are strained to 24 mm at a rate of 1 mms⁻¹, held at that displacement for 30 s, and returned to the zero-displacement condition. The increase in stiffness in the foil-elastomer samples is also observed. The foil-elastomer samples also have a higher degree of hysteresis (14-19%) between loading and unloading as compared to the elastomer only samples (<5%).

The deformation of each foil-elastomer pattern is presented in a series of photographs (Fig. 6). In both x and y, the increasing length and width and unfolding of the pattern can be observed at maximum strain. An increase in electrode gaps, indicating elastomer stretch rather than unfolding, is also observable in patterns A and B at maximum strain.

3.2 Capacitance response

During the foil-elastomer strain response tests, capacitance is measured using a capacitance to digital board (AD7745, Analog Devices). The initial average capacitance of A, B, and C are 17.9 pF, 17.5 pF, and 17.9 pF, respectively, with standard deviations of 1.2 pF, 0.6 pF, and 1.0 pF, respectively. While pattern C has the smallest electrode gaps due to low θ , the pattern faces are smaller because α is smaller, so the nominal capacitances of all patterns are within 500 fF of one another.

As each pattern is strained, the electrodes move further away from one another, and the capacitance decreases (Fig. 7). The mean of each data set is shown with the bold line, and one standard deviation is shown with the shaded region. In the x axis, the largest sensitivity occurs for pattern A, and the smallest sensitivity for pattern C. The x axis behavior is in contrast with

the y axis response, where all three patterns have similar sensitivities. Pattern A has a very large variation in sensitivity, likely due to variations in the electrode alignment and therefore initial capacitance.

The relative sensitivity has an inverse relationship from the prediction of the Miura models presented earlier. Pattern A has the lowest ratio of y/x sensitivity, approximately 0.24 at 20% strain, while C has the highest (~ 0.75 at 20% strain), and pattern B has a sensitivity ratio of 0.34. At 5% strain, the sensitivity ratios were 0.32, 0.35, and 0.49 for A, B, and C, respectively. In contrast, the model predicted sensitivity ratios of 2.3, 0.71, and 0.34 for A, B, and C, respectively, for a κ_x value of 0.5. Potential explanations for this opposing trend in C_y/C_x sensitivity ratios are presented in the discussion section.

The behavior of pattern A under cyclic deformation is shown in Fig. 8. The pattern is strained to 20% over 600 cycles in a series of slow (0.25 mms⁻¹ or 0.33%s⁻¹), moderate (0.75 mms⁻¹ or 1%s⁻¹), and fast (2.25 mms⁻¹ or 3%s⁻¹) rates. The inset figures show an elastomer-only sample and a foil-elastomer sample during cycles 94-96 and 597-599. Both samples mechanically and electrically withstand the 600 cycles. The response of the elastomer-only sample is stable across the test, with no changes in stiffness or evidence of slipping from the tester grip.

The foil-elastomer sample partially slips from the tester grip on the first cycle, resulting in a negative (compressive) force at zero displacement after the first cycle. The compliance remains constant across the three speeds in one series of slow-moderate-fast tests and increases by less than 5% from the first to the 600th cycle. The capacitance of the foil-elastomer sample decreases during the test and reaches a minimum capacitance decrease of 19% at 20% strain. Once the cyclic test is complete, the capacitance increases but does not recover to its initial value.

4 Discussion

The foil-elastomer devices do show modified properties with initial fold angle, in both the mechanical and capacitive responses. Because the elastomer-only devices may easily deform at both the faces and folds, the pattern angle does not appreciably change its strain response. Adding an inextensible layer (the foil electrodes) eliminates stretching at the faces. Due to the fabrication process, the folds may stretch in x because there is no foil electrode present between opposing faces. In y, foil is present at the fold between cells in order to electrically connect them. To realize greater stiffness tuning, inextensible materials or other approaches that enforce unfolding over stretching should be integrated into all pattern angles.

Although the inextensible foil creates tunability, it presents challenges in realizing high stability and precision. During loading and unloading, the foil-elastomer samples experience more than three times the hysteresis of their elastomer-only counterparts. Because silicone does not form a strong bond with aluminum as it cures, the hysteresis may reflect that the elastomer is moving relative to the foil as it is strained. Improving the adhesion between elastomer and electrode, either through a stiffness gradient, through material selection, or using an adhesion promoter such as Silpoxy may reduce the amount of hysteresis by causing the pattern to deform as a unified body.

The strain sensitivity is also tunable with the pattern angles: the most planar device with the largest angles (A) has the lowest ratio of y-to-x sensitivity, while the most three-dimensional pattern with the smallest angles (C) has the highest ratio of y-to-x

sensitivity. Although the target performance for a soft sensor will vary based on the application, the high anisotropy observed in pattern C would make a good candidate for rejecting off-axis strain. Furthermore, the overall tuning ability between patterns supports further investigation for origami-patterned sensors that may be reconfigured to change their properties (e.g., using shape-changing materials).

The analytical model does not accurately predict the trend or relative sensitivity ratios, likely due to two factors. The model accounts for material stretching at the joint through a constant value of κ_x . However, this value of κ_x is not likely to be constant across all α , θ sets, as the fold stiffnesses change with selection of pattern angles [21]. Future models of cell deformation must account for fold stiffnesses to determine an appropriate κ_x value.

The model also ignores the effects of the fringing field, which will change with the initial pattern angle and as the electrodes move. More tightly folded structures (e.g., pattern C) more closely approximate a parallel plate, while the model would not accurately capture the fringing field in more planar patterns. Finite element modeling will likely be required to capture the hyper-elastic material deformation and fringing field aspects of the origami-patterned sensors.

5 Conclusion

We presented an origami-patterned, capacitive strain sensor with tunable electrical and mechanical properties based on the fabricated fold angles, with y-to-x strain sensitivity ratios from 0.5 to 0.2 based on fabricated pattern angle. The mechanical responses of samples with and without inextensible foil layers suggest that angles within origami-patterned structures must fold and unfold, rather than stretch, in order to preserve the mechanical properties for which origami is prized.

Preserving folding and unfolding behaviors in stretchable materials poses both design and materials challenges to be investigated in future work. Multi-physics finite element simulation tools may aid in determining appropriate materials, fold designs, and pattern geometries for more precise tuning. Integrating sensing modalities into origami-patterned actuators and designing origami sensors with stiffness-tuned joints will enable such devices to have tunable, reconfigurable, actuation, and sensing within one system. Origami-patterned soft sensors show promise for future soft sensors with programmed properties, as well for sensing the position of origami-patterned actuators and soft robots for closed-loop control.

Acknowledgements

This work was supported by NSF CAREER award 1846954. The authors thank Dale Renfrow and Eric Jensen for guidance with mold printing. K.L.D. thanks Peter Klemperer and R. Jordan Crouser for assistance with the custom CAD script.

References

[1] M. Schenk and S. D. Guest, "Geometry of miura-folded metamaterials," *Proceedings of the National Academy of Sciences*, vol. 110, no. 9, pp. 3276–3281, 2013. [Online]. Available: http://www.pnas.org/content/110/9/3276

- [2] W.-H. Chen, S. Misra, Y. Gao, Y.-J. Lee, D. E. Koditschek, S. Yang, and C. R. Sung, "A Programmably Compliant Origami Mechanism for Dynamically Dexterous Robots," *IEEE Robotics and Automation Letters*, vol. 5, no. 2, pp. 2131–2137, Apr. 2020, conference Name: IEEE Robotics and Automation Letters.
- [3] S. Li, D. M. Vogt, D. Rus, and R. J. Wood, "Fluid-driven origami-inspired artificial muscles," *Proceedings of the National Academy of Sciences*, vol. 114, no. 50, pp. 13132–13137, Dec. 2017, publisher: National Academy of Sciences Section: Physical Sciences. [Online]. Available: https://www.pnas.org/content/114/50/13132
- [4] C. D. Onal, R. J. Wood, and D. Rus, "An Origami-Inspired Approach to Worm Robots," *IEEE/ASME Transactions on Mechatronics*, vol. 18, no. 2, pp. 430–438, Apr. 2013, conference Name: IEEE/ASME Transactions on Mechatronics.
- [5] M. T. Tolley, S. M. Felton, S. Miyashita, D. Aukes, D. Rus, and R. J. Wood, "Self-folding origami: shape memory composites activated by uniform heating," *Smart Materials and Structures*, vol. 23, no. 9, p. 094006, Aug. 2014, number: 9 Publisher: IOP Publishing. [Online]. Available: https://doi.org/10.1088/0964-1726/23/9/094006
- [6] R. V. Martinez, C. R. Fish, X. Chen, and G. M. Whitesides, "Elastomeric Origami: Programmable Paper-Elastomer Composites as Pneumatic Actuators," *Advanced Functional Materials*, vol. 22, no. 7, pp. 1376–1384, 2012, _eprint: https://onlinelibrary.wiley.com/doi/pdf/10.1002/adfm.201102978. [Online]. Available: https://onlinelibrary.wiley.com/doi/abs/10.1002/adfm.201102978
- [7] M. A. Robertson, O. C. Kara, and J. Paik, "Soft pneumatic actuator-driven origami-inspired modular robotic "pneumagami"," *The International Journal of Robotics Research*, vol. 40, no. 1, pp. 72–85, Jan. 2021, publisher: SAGE Publications Ltd STM. [Online]. Available: https://doi.org/10.1177/0278364920909905
- [8] S. Zhang, X. Ke, Q. Jiang, H. Ding, and Z. Wu, "Programmable and reprocessable multifunctional elastomeric sheets for soft origami robots," *Science Robotics*, vol. 6, no. 53, p. eabd6107, Apr. 2021, publisher: American Association for the Advancement of Science. [Online]. Available: https://www.science.org/doi/full/10.1126/scirobotics.abd6107
- [9] A. Firouzeh and J. Paik, "Robogami: A Fully Integrated Low-Profile Robotic Origami," *Journal of Mechanisms and Robotics*, vol. 7, no. 2, May 2015. [Online]. Available: https://doi.org/10.1115/1.4029491
- [10] T.-H. Kim, J. Vanloo, and W. S. Kim, "3D Origami Sensing Robots for Cooperative Health-care Monitoring," *Advanced Materials Technologies*, vol. 6, no. 3, p. 2000938, 2021, _eprint: https://onlinelibrary.wiley.com/doi/abs/10.1002/admt.202000938. [Online]. Available: https://onlinelibrary.wiley.com/doi/abs/10.1002/admt.202000938
- [11] T. Mori and H. Onoe, "Shape-Recognizable Origami Sheet Device With Single Walled Carbon Nanotube Strain Sensor," *Journal of Microelectromechanical Systems*, vol. 30, no. 2, pp. 234–242, Apr. 2021, number: 2 Conference Name: Journal of Microelectromechanical Systems.
- [12] J. Shintake, T. Nagai, and K. Ogishima, "Sensitivity Improvement of Highly Stretchable Capacitive Strain Sensors by Hierarchical Auxetic Structures," *Frontiers in Robotics and AI*, vol. 6, 2019. [Online]. Available: https://www.frontiersin.org/articles/10.3389/frobt.2019.00127/full
- [13] Y.-J. Lee, S.-M. Lim, S.-M. Yi, J.-H. Lee, S.-g. Kang, G.-M. Choi, H. N. Han, J.-Y. Sun, I.-S. Choi, and Y.-C. Joo, "Auxetic elastomers: Mechanically programmable meta-elastomers with an unusual Poisson's ratio overcome the gauge limit of a capacitive type strain sensor," *Extreme Mechanics Letters*, vol. 31, p. 100516, Sep. 2019. [Online]. Available: http://www.sciencedirect.com/science/article/pii/S2352431619300409
- [14] K. L. Dorsey, "Reconfigurable soft capacitive sensor with variable stiffness ring," in 2019 2nd IEEE International Conference on Soft Robotics (RoboSoft), 2019, pp. 378–383.
- [15] S. Xu, D. M. Vogt, W.-H. Hsu, J. Osborne, T. Walsh, J. R. Foster, S. K. Sullivan, V. C. Smith, A. W. Rousing, E. C. Goldfield, and R. J. Wood, "Biocompatible Soft Fluidic Strain and Force Sensors for Wearable Devices," *Advanced Functional Materials*, vol. 29, no. 7, p. 1807058, 2019, number: 7. [Online]. Available: https://onlinelibrary.wiley.com/doi/abs/10.1002/adfm.201807058
- [16] R. Xie, S. Hou, Y. Chen, K. Zhang, B. Zou, Y. Liu, J. Liang, S. Guo, H. Li, B. Zheng, S. Li, W. Zhang, J. Wu, and F. Huo, "Leather-based strain sensor with hierarchical structure for motion monitoring," *Advanced Materials Technologies*, vol. 4, no. 10, p. 1900442, 2019.

- [17] K. L. Dorsey, M. Cao, G. A. Slipher, and N. Lazarus, "Mechanical isolation and temperature compensation in soft elastomer components," *IEEE J. Sensors*, vol. 18, no. 18, pp. 7505–7512, 2018.
- [18] W. Cheng, J. Wang, Z. Ma, K. Yan, Y. Wang, H. Wang, S. Li, Y. Li, L. Pan, and Y. Shi, "Flexible Pressure Sensor with High Sensitivity and Low Hysteresis Based on a Hierarchically Microstructured Electrode," *IEEE Electron Device Letters*, vol. PP, no. 99, pp. 1–1, 2017, number: 99.
- [19] A. Dwivedi, A. Ramakrishnan, A. Reddy, K. Patel, S. Ozel, and C. D. Onal, "Design, Modeling, and Validation of a Soft Magnetic 3-D Force Sensor," *IEEE Sensors Journal*, vol. 18, no. 9, pp. 3852–3863, May 2018, number: 9.
- [20] A. Baldwin and E. Meng, "Kirigami Strain Sensors Microfabricated From Thin-Film Parylene C," *Journal of Microelectromechanical Systems*, vol. 27, no. 6, pp. 1082–1088, Dec. 2018, number: 6.
- [21] Z. Y. Wei, Z. V. Guo, L. Dudte, H. Y. Liang, and L. Mahadevan, "Geometric Mechanics of Periodic Pleated Origami," *Physical Review Letters*, vol. 110, no. 21, p. 215501, May 2013. [Online]. Available: https://link.aps.org/doi/10.1103/PhysRevLett.110.215501
- [22] S. W. Grey, F. Scarpa, and M. Schenk, "Strain Reversal in Actuated Origami Structures," *Physical Review Letters*, vol. 123, no. 2, p. 025501, Jul. 2019, publisher: American Physical Society. [Online]. Available: https://link.aps.org/doi/10.1103/PhysRevLett.123.025501
- [23] J. L. Silverberg, A. A. Evans, L. McLeod, R. C. Hayward, T. Hull, C. D. Santangelo, and I. Cohen, "Using origami design principles to fold reprogrammable mechanical metamaterials," *Science*, vol. 345, no. 6197, pp. 647–650, Aug. 2014. [Online]. Available: http://science.sciencemag.org/content/345/6197/647
- [24] K. Saito, A. Tsukahara, and Y. Okabe, "New Deployable Structures Based on an Elastic Origami Model," *Journal of Mechanical Design*, vol. 137, no. 2, Feb. 2015. [Online]. Available: https://doi.org/10.1115/1.4029228
- [25] J. Yi, X. Chen, C. Song, J. Zhou, Y. Liu, S. Liu, and Z. Wang, "Customizable Three-Dimensional-Printed Origami Soft Robotic Joint With Effective Behavior Shaping for Safe Interactions," *IEEE Transactions on Robotics*, vol. 35, no. 1, pp. 114–123, Feb. 2019, conference Name: IEEE Transactions on Robotics.
- [26] J. Kaufmann, P. Bhovad, and S. Li, "Harnessing the Multistability of Kresling Origami for Reconfigurable Articulation in Soft Robotic Arms," *Soft Robotics*, Feb. 2021, publisher: Mary Ann Liebert, Inc., publishers. [Online]. Available: https://www.liebertpub.com/doi/full/10.1089/soro.2020.0075
- [27] S. Wu, Q. Ze, J. Dai, N. Udipi, G. H. Paulino, and R. Zhao, "Stretchable origami robotic arm with omnidirectional bending and twisting," *Proceedings of the National Academy of Sciences*, vol. 118, no. 36, Sep. 2021, publisher: National Academy of Sciences Section: Physical Sciences. [Online]. Available: https://www.pnas.org/content/118/36/e2110023118
- [28] S. Liu, Z. Fang, J. Liu, K. Tang, J. Luo, J. Yi, X. Hu, and Z. Wang, "A Compact Soft Robotic Wrist Brace With Origami Actuators," *Frontiers in Robotics and AI*, vol. 8, p. 34, 2021. [Online]. Available: https://www.frontiersin.org/article/10.3389/frobt.2021.614623
- [29] C. Göttler, K. Elflein, R. Siegwart, and M. Sitti, "Spider Origami: Folding Principle of Jumping Spider Leg Joints for Bioinspired Fluidic Actuators," *Advanced Science*, vol. 8, no. 5, p. 2003890, 2021, _eprint: https://onlinelibrary.wiley.com/doi/pdf/10.1002/advs.202003890. [Online]. Available: https://onlinelibrary.wiley.com/doi/abs/10.1002/advs.202003890
- [30] T. Jin, L. Li, T. Wang, G. Wang, J. Cai, Y. Tian, and Q. Zhang, "Origami-Inspired Soft Actuators for Stimulus Perception and Crawling Robot Applications," *IEEE Transactions on Robotics*, pp. 1–17, 2021, conference Name: IEEE Transactions on Robotics.
- [31] W. Kim, J. Byun, J.-K. Kim, W.-Y. Choi, K. Jakobsen, J. Jakobsen, D.-Y. Lee, and K.-J. Cho, "Bioinspired dual-morphing stretchable origami," *Science Robotics*, vol. 4, no. 36, p. eaay3493, Nov. 2019, publisher: American Association for the Advancement of Science. [Online]. Available: https://www.science.org/doi/10.1126/scirobotics.aay3493
- [32] L. Paez, G. Agarwal, and J. Paik, "Design and Analysis of a Soft Pneumatic Actuator with Origami Shell Reinforcement," *Soft Robotics*, vol. 3, no. 3, pp. 109–119, Sep. 2016, publisher: Mary Ann Liebert, Inc., publishers. [Online]. Available: https://www.liebertpub.com/doi/full/10.1089/soro.2016.0023

- [33] K. Miura, "The Science of Miura-Ori: A Review," in *Origami 4*. CRC Press, Aug. 2009, pp. 87–99, google-Books-ID: kOPqBgAAQBAJ.
- [34] J.-H. Na, A. A. Evans, J. Bae, M. C. Chiappelli, C. D. Santangelo, R. J. Lang, T. C. Hull, and R. C. Hayward, "Programming Reversibly Self-Folding Origami with Micropatterned Photo-Crosslinkable Polymer Trilayers," *Advanced Materials*, vol. 27, no. 1, pp. 79–85, Jan. 2015, number: 1. [Online]. Available: http://onlinelibrary.wiley.com/doi/10.1002/adma.201403510/abstract
- [35] C. D. Santangelo, "Extreme Mechanics: Self-Folding Origami," *Annual Review of Condensed Matter Physics*, vol. 8, no. 1, pp. 165–183, 2017, number: 1. [Online]. Available: https://doi.org/10.1146/annurev-conmatphys-031016-025316
- [36] T. H. Hong, S.-H. Park, J.-H. Park, N.-J. Paik, and Y.-L. Park, "Design of Pneumatic Origami Muscle Actuators (POMAs) for A Soft Robotic Hand Orthosis for Grasping Assistance," in 2020 3rd IEEE International Conference on Soft Robotics (RoboSoft), May 2020, pp. 627–632.
- [37] J. Ma, J. Song, and Y. Chen, "An origami-inspired structure with graded stiffness," *International Journal of Mechanical Sciences*, vol. 136, pp. 134–142, Feb. 2018. [Online]. Available: http://www.sciencedirect.com/science/article/pii/S0020740317332599
- [38] S. Li, J. J. Stampfli, H. J. Xu, E. Malkin, E. V. Diaz, D. Rus, and R. J. Wood, "A Vacuum-driven Origami "Magic-ball" Soft Gripper," in 2019 International Conference on Robotics and Automation (ICRA), May 2019, pp. 7401–7408, iSSN: 2577-087X.
- [39] M. Gardiner, R. Aigner, H. Ogawa, E. Reitbock, and R. Hanlon, "Fold Printing: Using Digital Fabrication of Multi-Materials for Advanced Origami Prototyping," in *Proceedings of the 7th Origami Science Mathematics and Education Conference*, 2018, p. 13.

Table 1: Pattern angles and capacitance ratio with κ value

Design	α	θ		$\Delta C_y / \Delta C_x$	
			$\kappa_x = 0.05$	$\kappa_x = 0.5$	$\kappa_x = 0.95$
A	65°	135°	2.6	2.3	2.1
В	55°	110°	0.90	0.91	0.92
C	45°	85°	0.32	0.34	0.37

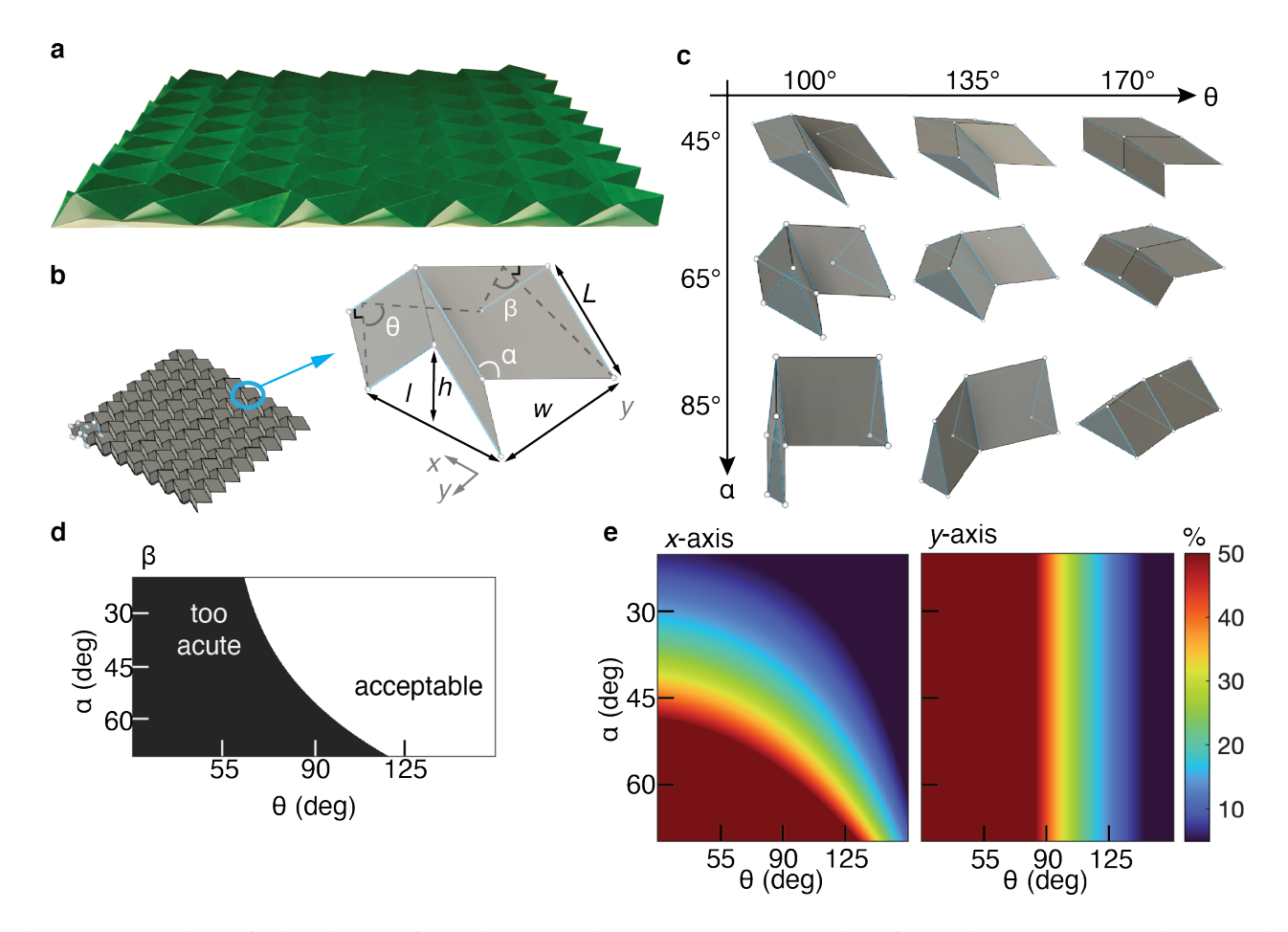


Figure 1: (a) A piece of origami paper folded into the Miura pattern. (b) A drawing of the Miura pattern, with eight cells in width and eight cells in length. The callout is one Miura cell with the pattern variables shown. (c) Drawings of Miura cells with varying α and θ . L is held constant. (d) A plot of angle β for α and θ . Fabricated patterns must have $\beta > 60^{\circ}$ to reliably fabricate. The shaded region shows α and θ which result in a β angle that is too acute to practically fabricate, and the unshaded region contains α, θ pairs that may be fabricated. (e) A heatmap of the maximum strain possible before reaching a planar sheet for each α, θ pair.

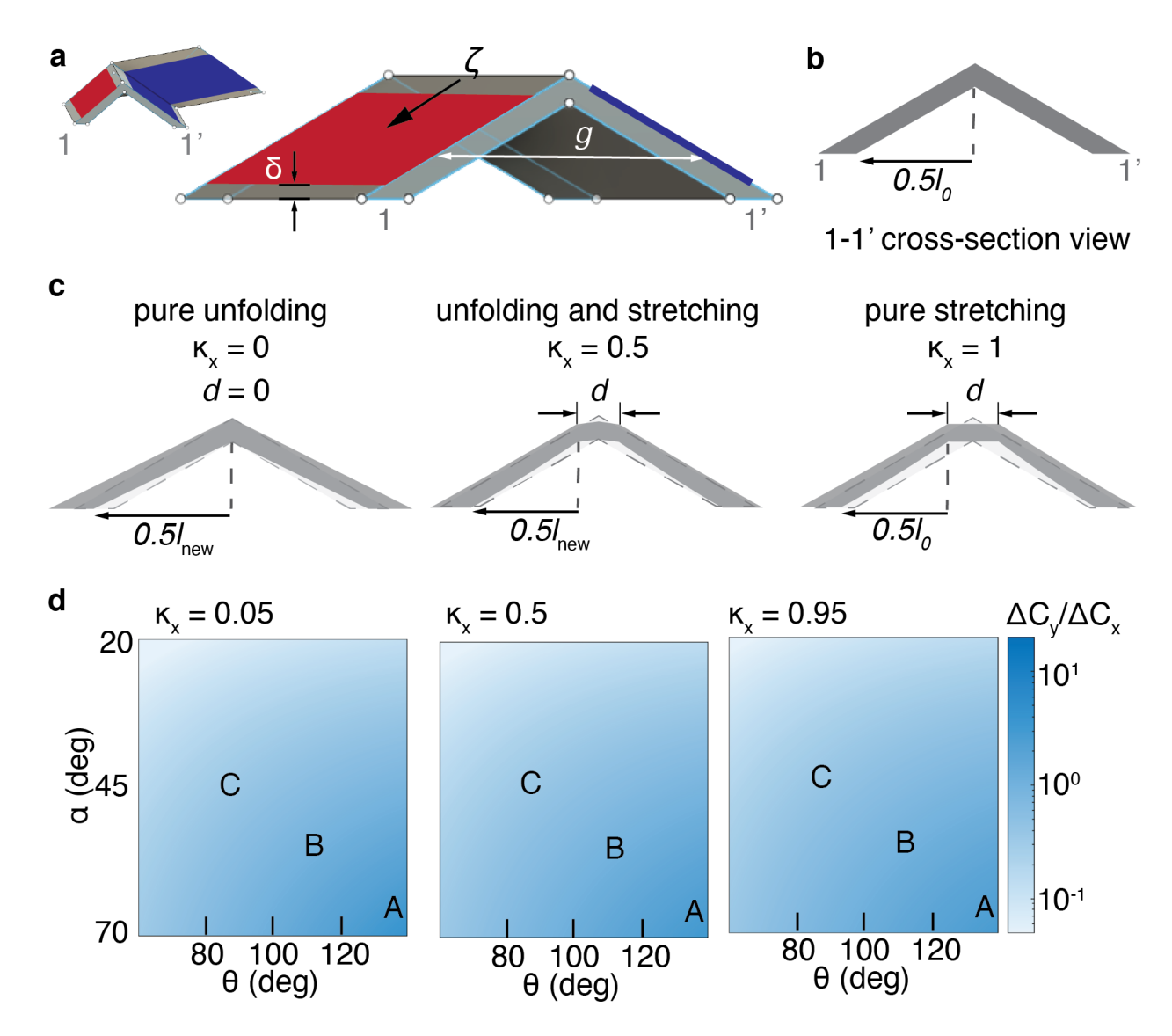


Figure 2: (a) Isometric and cross-sectional drawings of one Miura cell with electrodes shown in red and blue. Capacitor variables and the 1-1' cross-section are shown. (b) The 1-1' cross-section of the Miura pattern. (c) Drawings of the cell deformation along the 1-1' cross-section as the cell unfolds (left, $\kappa=0$), unfolds and stretches (center, $\kappa=0.5$), and stretches (right, $\kappa=1$). (d) Predictions of the relative change in capacitance $\Delta C_y/\Delta C_x$ for a strain of 5%, with letters A, B, and C on the heatmaps denoting the selected initial α, θ combinations for the fabricated patterns. The ratio between stretching and unfolding is indicated by κ , where $\kappa=0$ is pure unfolding.

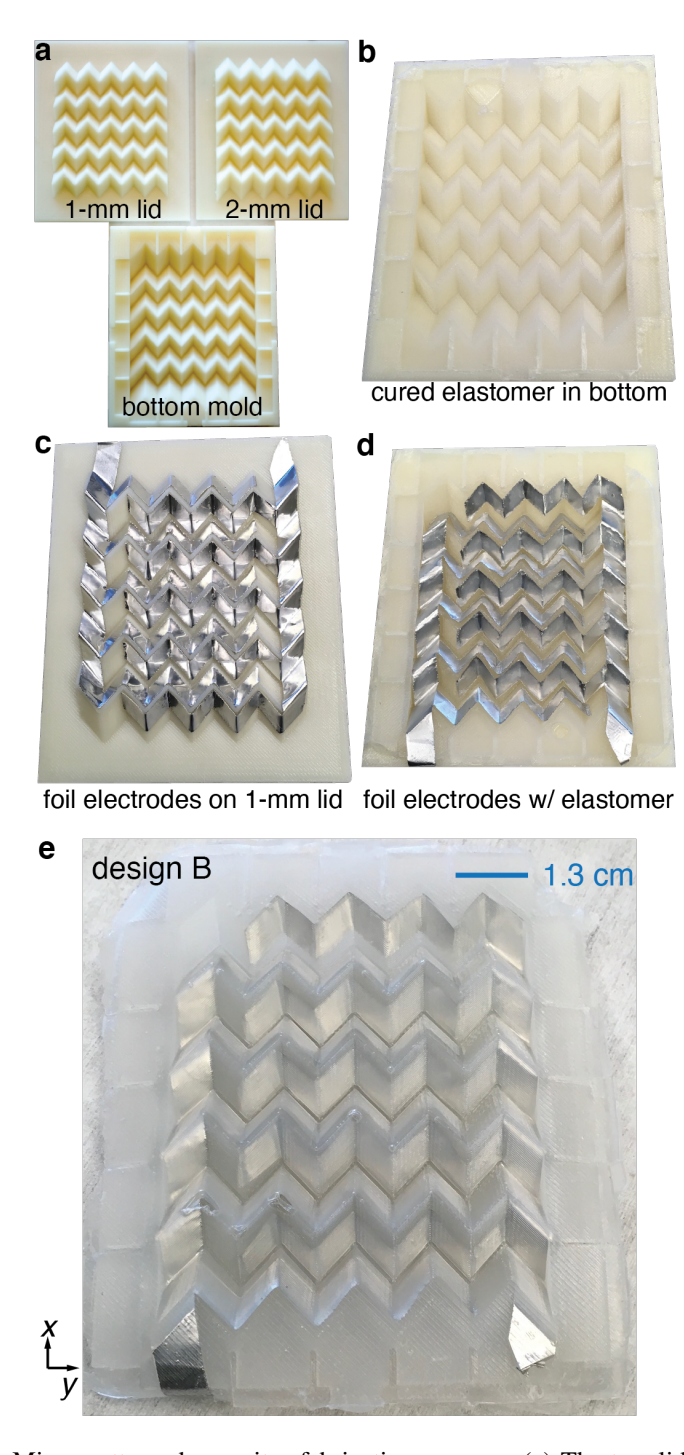


Figure 3: Photographs of the Miura-patterned capacitor fabrication process. (a) The two lids and bottom 3D printed molds before elastomer introduction of pattern B. (b) After the first silicone molding step, with a design B pattern, creating a 1 mm thick pattern. (c) The foil electrodes adhered to the thinner upper mold. (d) The foil electrodes adhered to the molded silicone. (e) A completed design B capacitor.

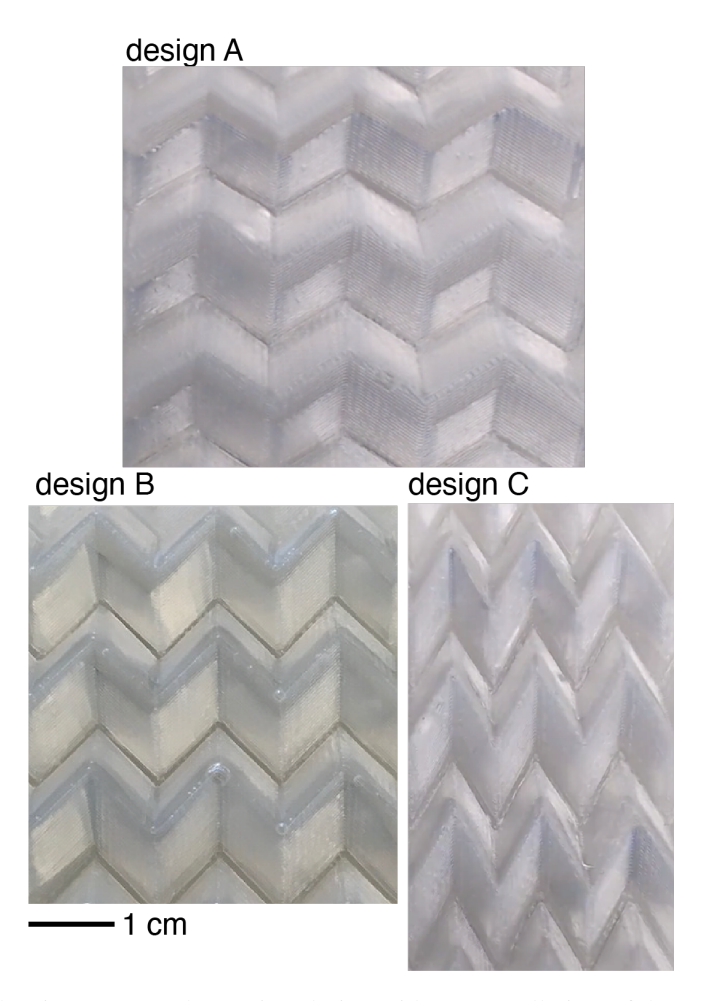


Figure 4: Photographs of each Miura-patterned capacitor design with a 3×3 cell view of the A, B, and C patterns after fabrication. The scale is constant across these photographs.

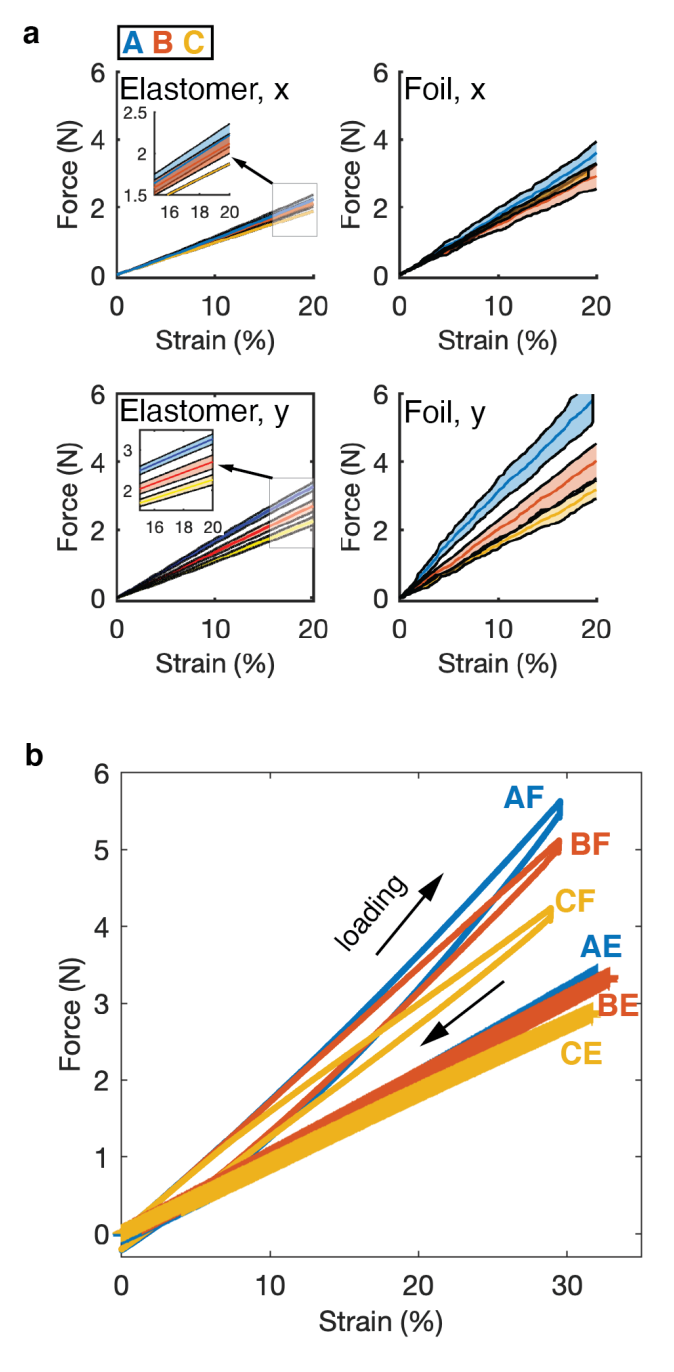


Figure 5: The mechanical response of each pattern. The bolded lines show the mean of each data set, and the shaded areas show one standard deviation from the mean. (a) Measured x (top) and y (bottom) strain response for elastomer (AE, BE, CE, left) and foil-elastomer (AF, BF, CF, right) devices. (b) A representative x axis loading and unloading cycle for each pattern. The elastomer-only samples show little hysteresis when compared to the foil-elastomer samples.

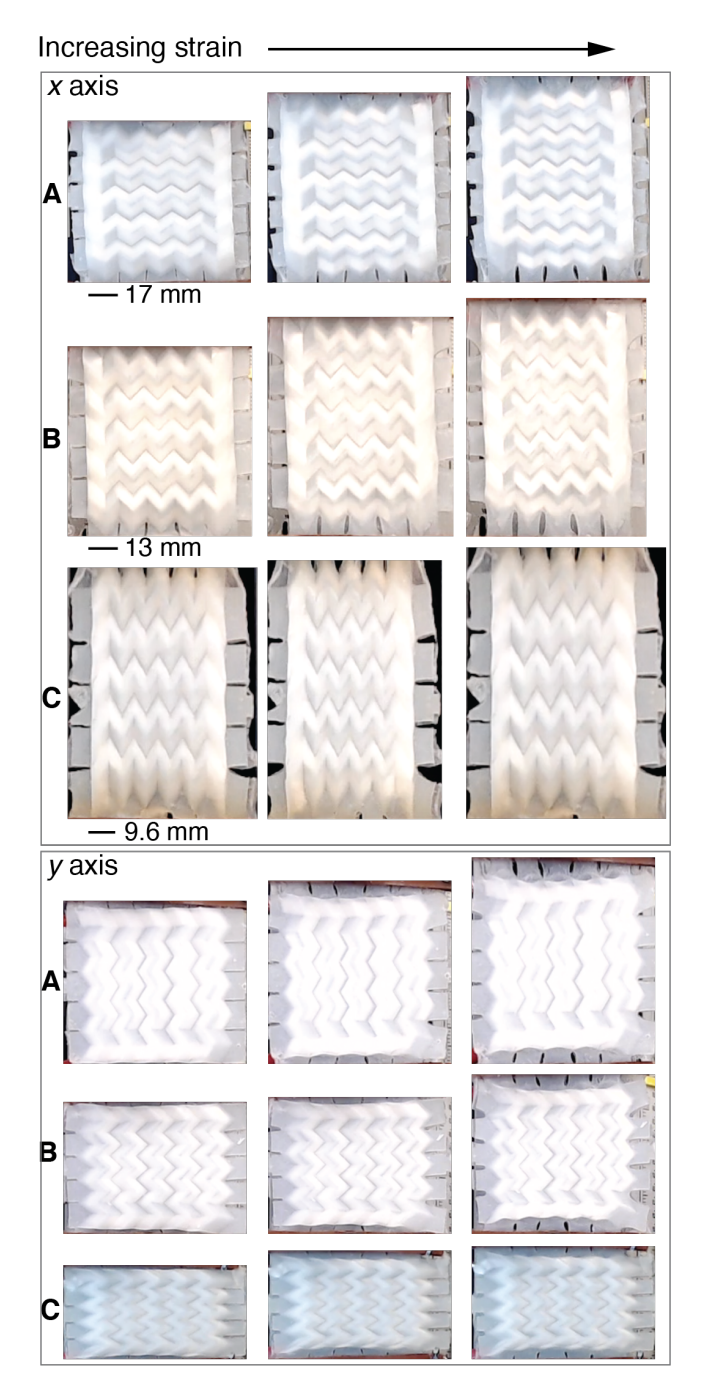


Figure 6: Photographs of each foil-elastomer pattern at no displacement (0 mm), halfway through the test (13 mm), and at the end of the test (26 mm). The C pattern was displaced to a maximum of 12 mm in y due to its narrower width. The auxetic behavior of the pattern (expansion in both x and y axes) is visible, along with an increase in elastomer spacing between the foil electrodes that suggests both unfolding and stretching behavior.

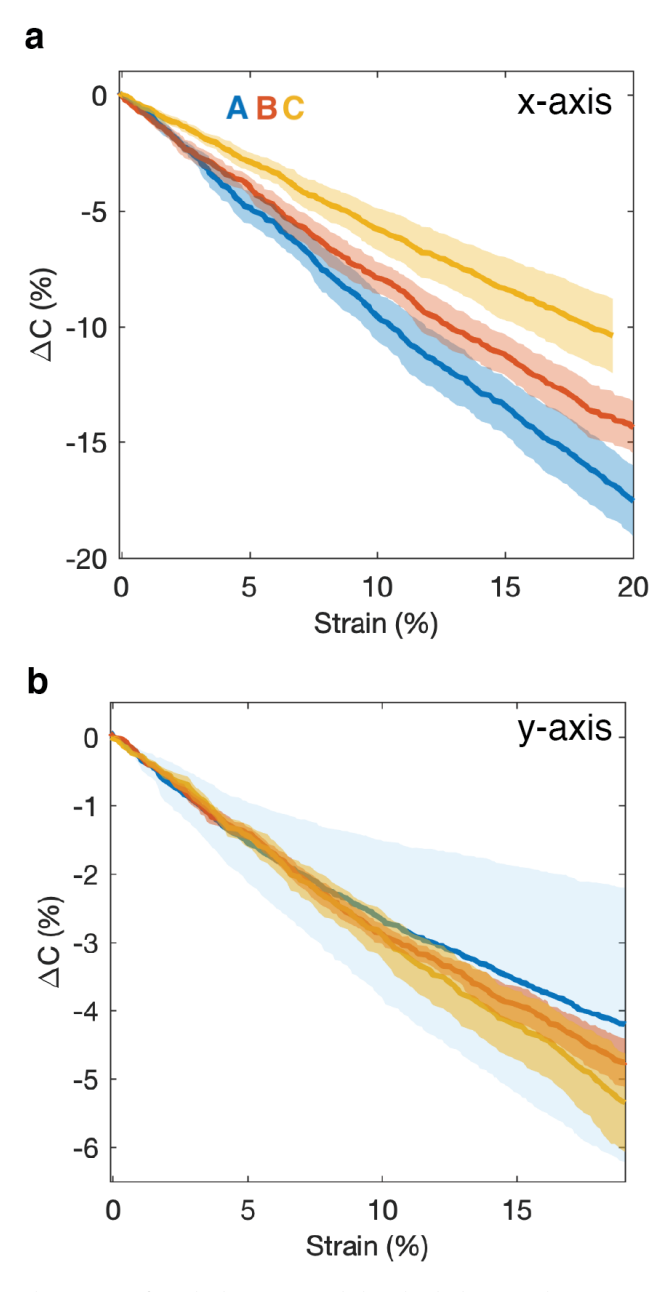


Figure 7: The bolded lines show the mean of each data set, and the shaded areas show one standard deviation from the mean. The capacitance of each pattern during strain tests in (a) x and (b) y, reported as a change in capacitance from the zero-displacement value and normalized to the zero-displacement value.

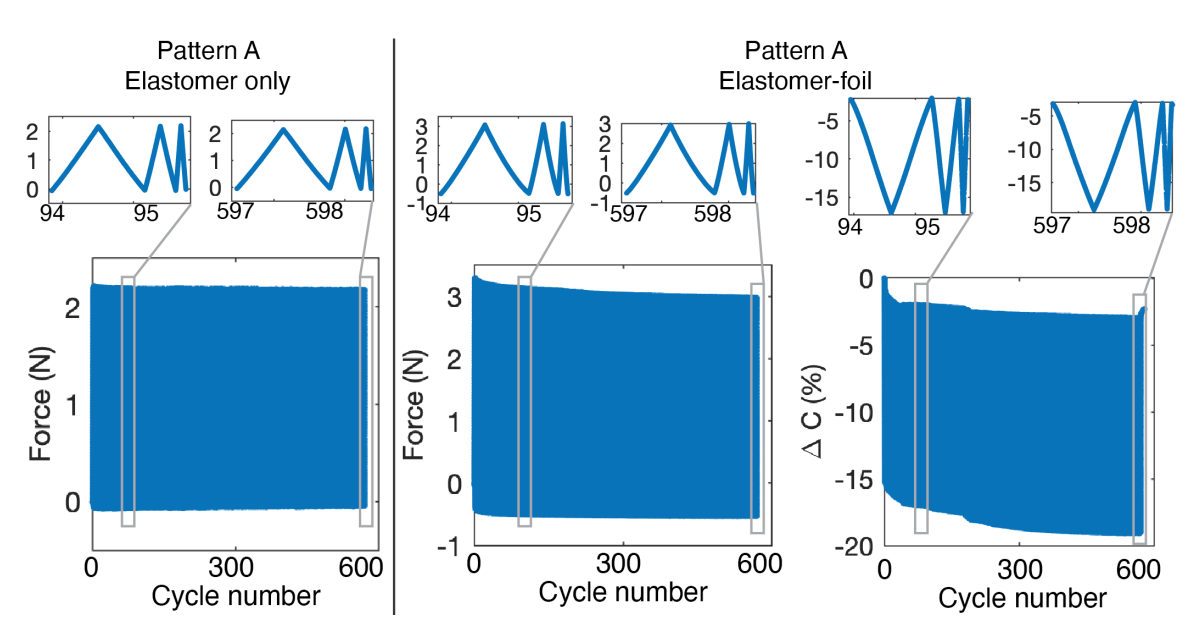


Figure 8: The behavior of elastomer-only and foil-elastomer samples of pattern A over 600 cycles at sequential strain rates of 0.33, 1, and 3%s⁻¹. The mechanical response of an elastomer only device is shown on the left, while the mechanical and capacitance response are shown on the right for an foil-elastomer device. Inset plots show one set of increasing strain rate cycles for each sample at cycle 100 and the last three cycles. The foil-elastomer sample is less stable with cyclic loading than the elastomer-only sample.